ACCSCIENCE PUBLISHING

Journal of Seismic Exploration

ARTICLE

Natural-source seismic frequency imaging for shallow-strata characterization of pow-er-transmission tower foundations in mountainous terrain

Wangxin Cai[1], Congyu Lin[1], Xiao Yang[2]*, and Jiahui Zuo[2]

[1]State Grid Fujian Economic Research Institute, Fuzhou, Fujian, China

[2]Geological Survey and Digital Earth (Beijing) Technology Co., Ltd., Beijing, China

Abstract

Reliable foundation design for power-transmission towers in mountainous terrain requires accurate knowledge of shallow weathering and bedrock geometry, yet steep relief, irregular bedrock, and uneven weathering limit point-based drilling and conventional surveys at the approximately 22 m × 22 m tower footprint. Here, natural-source seismic frequency imaging was adapted to this setting through a multi-constrained characteristic-frequency workflow, a diagonal-crossing observation system, and terrain-adaptive acquisition. Three survey grids comprising 138 stations were acquired in Minhou, Fujian, using 1 m receiver spacing and 20 min records. The resulting dimensionless normalized relative wave-impedance profiles delineated the silty-clay cover and completely, strongly, and moderately weathered tuff, including a site with 19 m internal relief. Against 13 interfaces from five boreholes, signed depth errors ranged from −0.80 to 1.20 m (root mean square error [RMSE] 0.61 m; mean absolute error [MAE] 0.53 m). Supplementary sensitivity analysis shows that velocity-prior and characteristic-frequency biases can produce depth errors comparable to the field residuals, whereas the chosen 1 m spacing contributes relatively small geometric interpolation error for interfaces varying over wavelengths of several meters. A geometry-only 3D sampling test further shows that the diagonal layout can miss small off-line bodies and therefore cannot replace true 3D investigation. The method is consequently best used as a borehole-calibrated, continuous-coverage complement for shallow foundation characterization rather than as a stand-alone lithology classifier.

Keywords: Power-transmission tower foundation; Complex mountainous terrain; Natural-source seismic frequency imaging; Ambient noise; Multi-constrained characteristic-frequency extraction; Diagonal-crossing observation system; Normalized relative wave impedance; Reliability evaluation

***Corresponding authors:**
Xiao Yang
(yangxiao@gsde.ltd)

Citation: Cai W, Lin C, Yang X, Zuo J. Natural-source seismic frequency imaging for shallow-strata characterization of pow-er-transmission tower foundations in mountainous terrain. *J Seismic Explor*.
doi: 10.36922/JSE026280136

Received: July 10, 2026

Revised: September 28, 2026

Accepted: September 28, 2026

Published online: October 26, 2026

Copyright: © 2026 Author(s). This is an Open-Access article distributed under the terms of the Creative Commons Attribution License, permitting distribution, and reproduction in any medium, provided the original work is properly cited.

Publisher's Note: AccScience Publishing remains neutral with regard to jurisdictional claims in published maps and institutional affiliations.

1. Introduction

Electric power grids are among the most critical pieces of energy infrastructure, and the stability of transmission-tower foundations directly governs the safe operation of overhead transmission lines. In the mountainous areas of Fujian Province and the wider southeastern coast of China, transmission lines frequently traverse low-to-medium-

relief, strongly dissected terrain. At such tower sites, a weathering crust and Quaternary slope-wash deposits of uneven thickness are widely developed and have been reshaped by prolonged tectonic activity and weathering erosion, so that the bedrock surface is highly irregular and the thickness of the overburden changes abruptly over short lateral distances. Accurately delineating the shallow stratigraphic structure beneath a tower, the thickness of the weathered layers, and the depth to bedrock is therefore a prerequisite for selecting a suitable bearing stratum and for rational foundation design and settlement control.[1,2] With more than 1,000 new towers added each year in the mountainous parts of Fujian, efficient and high-resolution site investigation under complex geological conditions has become an urgent need for power-engineering construction.

Conventional tower-foundation investigation relies mainly on drilling, cone penetration tests, standard penetration tests, and laboratory soil testing. Although these methods directly yield lithology and geotechnical parameters, they are intrinsically point-wise and discrete and cannot resolve the lateral continuity of stratigraphic interfaces. In rugged terrain, a single tower position commonly requires two to three days of integrated investigation, which is costly and time-consuming, and the limited accessibility of the sites makes borehole layout difficult. Mechanized construction can improve efficiency and reduce safety risks in mountainous areas, but it depends heavily on high-quality geological models; in Minhou County, the complex combination of strata makes it difficult for conventional discrete sampling to capture the spatial variation of the layers, posing a serious challenge to mechanized construction.[1] Thus, there is a pressing need for high-precision geophysical techniques that can rapidly provide continuous stratigraphic information to complement limited drilling.

Geophysical methods can image continuous subsurface structure without disturbing the strata and are widely used in engineering investigation. For the present problem, however—a small footprint combined with a relatively large target depth—the commonly used techniques each have limitations. Shallow seismic reflection can provide high resolution but requires active-source deployment that may be difficult in rugged terrain;[3] ground-penetrating radar performance is limited by penetration depth in conductive or heterogeneous ground, whereas electrical-resistivity images can smooth or ambiguously represent sharp shallow boundaries.[4,5] Magnetotelluric measurements are vulnerable to cultural and nonstationary noise,[6,7] and surface-wave inversions may smooth thin or gradational layers and require careful acquisition and interpretation.[8,9] Similar logistical and resolution trade-offs arise in urban subsurface investigations, where access, infrastructure, and the need to combine several nondestructive methods complicate field operations.[10-12] Consequently, reliable fine-scale characterization of near-surface structure remains a central challenge,[13] and high-resolution approaches designed for difficult near-surface targets are especially valuable.[14]

Natural-source seismic frequency imaging, as implemented here, is a passive-source approach that interprets stable spectral responses of the shallow subsurface. Related ambient-noise methods have demonstrated that shallow geology and bedrock-related structure can be characterized without an active source.[15] Comparable seismic or integrated geophysical strategies have also been applied in mineral exploration,[16] dense-array urban imaging,[17] and karst or sinkhole-prone terrain.[18] These studies generally address larger or differently configured survey areas; adaptation to the approximately 22 m × 22 m footprint of a transmission-tower platform and to complex mountainous terrain remains insufficiently standardized, particularly in observation-system design and acquisition-parameter selection.

To address these issues, this study uses a representative transmission-tower work area in Minhou, Fujian, as its subject and carries out natural-source seismic frequency imaging together with quantitative reliability and uncertainty evaluations. Five questions are addressed: (i) how to design an observation system that balances coverage and operational efficiency within an approximately 22 m × 22 m tower platform; (ii) how to robustly extract stratigraphic characteristic frequencies from complex ambient noise; (iii) under what physical conditions the quarter-wavelength resonance approximation is defensible, and how departures from these conditions propagate into thickness estimates; (iv) how noise, prior information, and spatial sampling influence the inversion uncertainty; and (v) what three-dimensional anomalies can be missed by the quasi-two-dimensional diagonal geometry. We combined multi-constrained frequency picking, diagonal-crossing acquisition, field-parameter tests, borehole validation, sensitivity analysis, and a geometry-only three-dimensional sampling experiment, using 138 stations across three survey grids and five boreholes.

2. Geological setting and engineering conditions

2.1. Regional geological background

The study area is located in Minhou County, Fujian Province, within the eastern Fujian volcanic depression of the South China fold belt, and the regional strata display

the typical tectonic character of the South China block. The basement is dominated by Yanshanian tuff overlain by Quaternary alluvial–slope-wash deposits; in the Fuzhou basin, this appears as a two-layer structure in which 50–200 m of alluvium overlies the tuff basement. Regional faulting is relatively well developed, but no Holocene active faults occur within 100 m of the proposed site, and the crustal stability is good, satisfying the site requirements for important power facilities.

2.2. Engineering geological conditions of the work area

The work area lies on the northwestern side of Maotian Village, Nanyu Town, Minhou County, on the northern piedmont of the Daiyun Mountains, where the landform is a piedmont alluvial–slope-wash terrace. Figure 1 shows the local work area and the positions of the three imaging survey grids (SK66, SK57-58, and SK1-5-12), with the two survey lines in each grid identified separately. As a result of prolonged tectonic activity, weathering, and erosion, the engineering geological conditions of the area are markedly complex, mainly in three respects:

(i) Pronounced topographic relief. The area lies in a piedmont transition zone with local slopes of 15°–20°, a typical shallowly dissected hilly landform that constrains the deployment of equipment and the layout of survey lines.

(ii) Large bedrock relief. Controlled by prolonged weathering, erosion, and tectonic reworking, the depth to the top of the Yanshanian tuff basement varies sharply in the lateral direction, with locally developed palaeo-erosion troughs and highs that cause abrupt changes in overburden thickness.

(iii) Uneven weathering-layer thickness. Governed by lithological contrasts and tectonic fracture zones, the thicknesses of the completely weathered and strongly weathered layers are highly unevenly distributed, intensifying the heterogeneity of the shallow stratigraphic structure.

These conditions make it difficult for conventional drilling to control lateral variation in the strata, while traditional geophysical methods do not provide sufficient resolution for fine shallow imaging; a high-precision shallow-detection technique suited to complex mountainous terrain is therefore required.

3. Materials and methods

3.1. Principle of natural-source seismic frequency imaging

The technique treats a stratum as a vibrating system with a defined thickness and elastic boundaries, whose natural frequency is controlled primarily by the layer thickness and the velocity. For a single soft layer resting on a hard



Figure 1. Location of the work area and deployment of the survey grids. The six survey-line identifiers are unique to their survey grid (L1 and L2 for each grid), and the map axes are expressed in geographic longitude and latitude.

basement, the fundamental resonance frequency, the shear-wave velocity, and the layer thickness approximately satisfy the quarter-wavelength relation:

$$f_0 \approx \frac{V_S}{4H} \tag{1}$$

where f_0 is the fundamental characteristic frequency of the layer (Hz), V_S is its shear-wave velocity (m/s), and H is the layer thickness (m). **Equation 1** shows that, for a fixed velocity, a thicker layer has a lower characteristic frequency. The interface depth can therefore be inverted from the measured characteristic frequency as:

$$H = \frac{V_S}{(4f_0)} \tag{2}$$

Equations 1 and **2** form the quantitative bridge among frequency, thickness, and velocity, and provide the theoretical basis for inverting stratigraphic structure from spectral information. When ambient sources such as ocean waves, wind, traffic, and machinery excite the ground, the time-domain signal recorded by the seismograph can be regarded as the convolution of the natural vibration response of the strata with the external vibration; transformed to the frequency domain, it can be written as:

$$X(f) = G(f)E(f) + N(f) \tag{3}$$

where $X(f)$ is the spectrum of the recorded signal, $G(f)$ is the site-related spectral response (whose peaks may represent effective resonant modes involving one or more layers), $E(f)$ is the spectrum of the external vibration, and $N(f)$ is the random-noise spectrum. The external vibration is strongly time-varying whereas the natural frequencies of the strata are relatively stable; statistical stacking and normalization of long, windowed time series therefore suppress the random noise $N(f)$ and the time-varying external term $E(f)$, allowing the structural response $G(f)$ to be expressed more consistently in the stacked spectrum. Imaging of the interfaces is based on the wave-impedance contrast between adjacent layers, the wave impedance being defined as the product of medium density and velocity:

$$Z = \rho V \tag{4}$$

where Z is the wave impedance, ρ is the density, and V is the velocity. The larger the impedance contrast across an interface, the stronger the corresponding frequency response. After the characteristic frequency and interface depth of each station have been extracted, a layer-stripping recursion successively removes the frequency contribution of the overlying layers, recovering the thickness of each layer and the relative elastic difference between layers; the relative wave impedance of each profile is then normalized profile by profile to obtain a dimensionless normalized relative wave impedance ranging from −10 to 10. It must be emphasized that this quantity is a dimensionless relative measure: it reflects the spatial distribution of the relative elastic differences between adjacent layers rather than the absolute wave impedance. Abrupt changes in its vertical gradient mark major stratigraphic interfaces; blue (low) values denote relatively low wave impedance and red (high) values relatively high wave impedance, on which basis interfaces can be identified and tracked laterally.

Compared with single-station resonance methods and the horizontal-to-vertical spectral ratio (HVSR),[19-21] the present technique uses ambient noise directly and requires no active source, making it better suited to complex mountainous sites; through array observation and layer stripping, it forms two-dimensional profiles and can resolve a multilayer structure comprising the overburden and the completely, strongly, and moderately weathered layers. Unlike surface-wave methods, which rely mainly on dispersion inversion,[22,23] its vertical resolving power is governed chiefly by the effective bandwidth, the inter-layer impedance contrast, and the frequency resolution, whereas the receiver spacing mainly affects the lateral characterization. The main limitations are that the imaging result is a relative quantity that is subject to a degree of non-uniqueness, so lithological interpretation must be calibrated against boreholes, and that applicability is restricted for very thick, loose overburden, for strong periodic cultural vibration, and for complex three-dimensional anomalies.

International studies provide the broader context for this positioning. The use of natural microseisms for passive reconnaissance was developed in array-estimator work on sedimentary basins.[24] Single-station microtremor and HVSR practice has since been consolidated through peer-reviewed reviews and resonance-focused methodological studies,[25,26] while reviews of ambient-noise wavefields emphasize the need to account for noise-source composition and wavefield stability.[27] Ambient-noise interferometry further shows that diffuse or ambient seismic fields can yield stable structural information through long-time averaging and correlation.[28,29] Surface-wave methods, which provide a complementary velocity-based framework for near-surface characterization, have also been systematized in tutorial and monograph studies.[30,31]

Equations 1 and **2** are an approximation, not a general multilayer inversion identity. Their clearest physical interpretation is for a laterally uniform or locally one-dimensional compliant layer over a substantially stiffer substrate, with approximately horizontal interfaces, linear

elastic response, a sufficiently stable shear-wave-related fundamental resonance, and an impedance contrast large enough to produce a distinguishable peak. Under these conditions, the quarter-wavelength relation links an effective resonance frequency to an effective travel time through the layer. HVSR and resonance studies likewise show that the inferred depth-frequency relation is site-dependent and becomes less reliable when lateral variations or two-dimensional resonances are important.[20,25,26,32]

For a one-dimensional stack of several layers, a more appropriate first-order travel-time form is:

$$f_0 \approx \left[4 \sum_i \frac{h_i}{V_{S,i}} \right]^{-1} \tag{5}$$

A spectral peak therefore represents the combined travel time of the participating stack unless a particular layer contribution is sufficiently separated to be isolated by the layer-stripping procedure. If interfaces dip, if velocity varies strongly laterally, or if local three-dimensional bodies occur, the measured spectrum can broaden, split, or shift because of directional resonance, edge effects, and mixed modes. In such cases, **Equation 2** returns an effective thickness rather than a unique geometric layer thickness, and a weak or shifted peak can be wrongly assigned to an interface. The geological-prior constraint reduces implausible assignments but cannot remove this physical non-uniqueness; borehole calibration remains necessary.

The first-order error propagation of **Equation 2** is:

$$\frac{\Delta H}{H} \approx \frac{\Delta V_S}{V_S} - \frac{\Delta f_0}{f_0} \tag{6}$$

Thus, a +5% bias in the adopted V_S produces approximately a +5% thickness bias, whereas a +5% frequency-pick bias produces $H/H_{true} = 1/1.05 = 0.952$, i.e., about a 4.8% underestimation. These sensitivity coefficients are used in Section 4.4 to place the field residuals in context. They also explain why the accuracy observed at the Minhou site should not be generalized without local velocity and borehole control.[32,33]

3.2. Multi-constrained robust extraction of characteristic frequencies

The raw field data are time series of vertical ground velocity at the surface, arising from both natural activity (e.g., ocean waves and wind) and cultural activity (e.g., traffic and machinery). The raw spectrum usually contains several peaks that include not only the resonance response of the strata but also environmental vibration and random noise. Conventional approaches pick the dominant spectral peak directly, which under the low signal-to-noise conditions of complex mountainous terrain can easily misidentify a spurious resonance as a stratigraphic characteristic frequency. To overcome this, we proposed a multi-constrained scheme for robust extraction of characteristic frequencies that integrates spectral-stability screening, geological prior constraints, and layer-stripping recursion into a workflow from the raw spectrum to the effective characteristic frequencies (Figure 2**;** Algorithm 1). The scheme comprises the following steps:

(i) Pre-processing. The raw time series are successively de-meaned, de-trended, and zero-phase band-pass filtered to confine the effective information to the 1–40 Hz target band; zero-phase filtering avoids phase distortion and preserves the temporal alignment of the signal.

(ii) Windowed spectral estimation. The pre-processed data are divided into 30 s windows with 50% overlap, and each window is tapered with a Hann window before a fast Fourier transform (FFT) is applied to obtain the amplitude spectrum to reduce spectral leakage.

(iii) Multi-window statistics and spectral-stability screening. The amplitude spectra of all windows within the long time series are stacked and normalized to obtain a stable power-spectral curve; the mean and standard deviation of the multi-window spectral energy are computed at each frequency, and only resonance peaks that are energetically stable and have a signal-to-noise ratio (SNR) greater than 3 are retained, which effectively suppresses random transient interference from vehicles and wind.

(iv) Geological prior constraints. A prior geological model is established from regional geological data and previous investigations; the constraints comprise reasonable thickness ranges for the principal units (overburden, completely weathered layer, strongly weathered layer) and a regional range of empirical shear-wave velocities. The thickness range corresponding to each candidate characteristic frequency is estimated from the upper and lower empirical-velocity bounds, and any candidate that departs markedly from the reasonable prior range is judged spurious and discarded. This use of geological prior information as a discrimination criterion is key to suppressing spurious resonances and improving the reliability of the picks.

(v) Layer-stripping recursion. For a multilayer structure, a top-down stripping strategy is adopted: the characteristic frequency of the shallowest layer is identified first and its thickness computed from **Equation 2**; the theoretical resonance energy of that

layer is then subtracted from the raw spectrum to obtain a residual spectrum, in which the characteristic frequency of the next layer is picked, and the procedure is repeated to extract the characteristic frequencies and thicknesses of the completely weathered, strongly weathered, and moderately weathered layers in turn. The process requires no iteration, is computationally efficient, and prevents weak deep signals from being masked by strong shallow energy.

(vi) Imaging output. The characteristic frequencies, interface depths, and inter-layer relative wave-impedance differences of all layers at all stations are combined and interpolated to generate a two-dimensional normalized relative wave-impedance profile.

3.3. Diagonal-crossing observation system for small work areas

The platform of a single transmission tower is typically about 22 m × 22 m, leaving limited space and making it impractical to lay out a large two-dimensional survey grid. To accommodate this constraint, we designed a diagonal-crossing observation system for small work areas (Figure 3). Survey lines were deployed along the two diagonals of the tower platform—denoted the L1–3 diagonal and the L2–4 diagonal (line 1 and line 2)—with the black triangles marking the acquisition stations along the diagonals. In practice, the nodes can be deployed and recorded along the two diagonals in two successive passes, and the equipment then recovered together; to ensure that the lines sample the strata directly beneath the tower legs, the layout was extended a suitable distance beyond the leg positions.

Relative to a single-line or multiple-parallel-line layout, the diagonal-crossing scheme has three advantages. First, it covers the four tower-leg areas and the platform center with a small number of stations; two parallel lines would require an additional central line to cover the middle of the platform, increasing both the number of stations and the operational cost. Second, the two lines share a redundant observation at their intersection, where agreement in interface depths provides an internal check on the consistency of the imaging. Third, the two profiles run in different directions and cross-validate each other, reducing the risk of direction-dependent artifacts. It should be noted that the scheme is essentially quasi-three-dimensional: the intersection provides only a single spatial constraint, the regions between the lines are not directly observed, and the ability to characterize local three-dimensional bodies (such

Algorithm 1. Multi-constrained robust extraction of characteristic frequencies

Input: vertical-component ambient-noise records; sampling rate; effective frequency band; regional empirical velocity range; prior layer-thickness ranges.
Output: characteristic frequency and interface depth of each layer; normalized relative wave-impedance profile.
Step 1 — Pre-processing: de-mean and de-trend the raw time series and apply a 1–40 Hz zero-phase band-pass filter.
Step 2 — Windowing: segment into 30 s windows with 50% overlap and apply a Hann taper to each segment.
Step 3 — Spectral estimation: compute the FFT amplitude spectrum of each window.
Step 4 — Multi-window statistics: stack and normalize all window spectra to obtain the power spectrum and the per-frequency mean and standard deviation.
Step 5 — Stability screening: retain candidate resonance peaks that are energetically stable and have SNR > 3.
Step 6 — Geological prior constraint: estimate the thickness of each candidate peak from the empirical velocity range and reject peaks that depart markedly from the prior thickness ranges.
Step 7 — Layer stripping: pick characteristic frequencies from shallow to deep, compute layer thickness from Equation 2, and subtract the theoretical resonance energy of each layer before processing the next.
Step 8 — Imaging output: combine the interface depths and inter-layer relative wave-impedance differences of all stations and interpolate to a two-dimensional normalized relative wave-impedance profile.

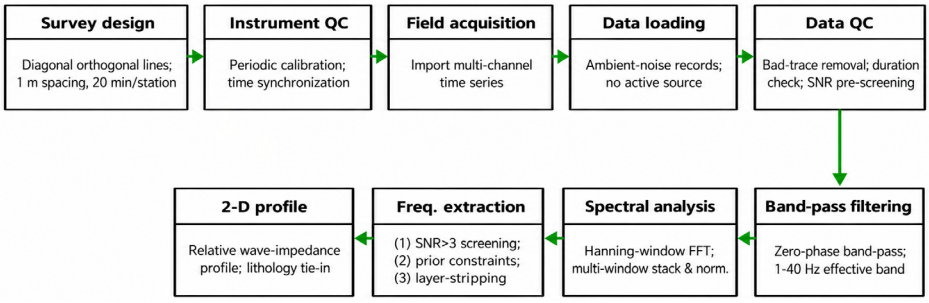


Figure 2. Workflow of the ambient-noise seismic frequency imaging technique
Abbreviations: FFT: Fast Fourier transform; QC: Quality check; SNR: Signal-to-noise ratio.

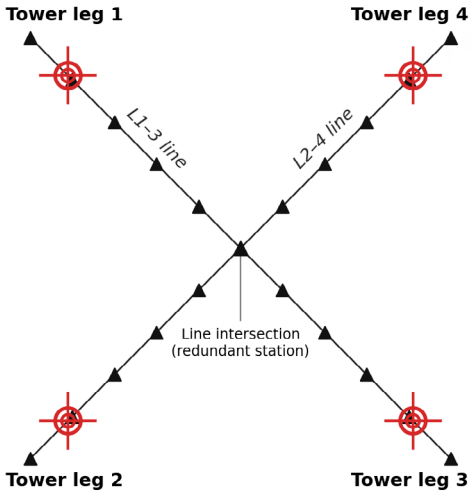


Figure 3. Layout of the diagonal-crossing survey lines at a tower position. The red targets mark the four tower legs, the black triangles mark the acquisition stations along the L1–3 and L2–4 diagonals, and the central station is the redundant observation at the line intersection.

as boulders or fracture zones) that may occur within the tower position is limited. For tower positions with complex geology or stringent three-dimensional requirements, the lines should be densified beyond the diagonal-crossing scheme, or the results combined with drilling and other geophysical methods; a two-dimensional profile cannot fully replace three-dimensional detection.

Because the two diagonals sample only two lines through the 22 m × 22 m platform, a numerical geometry test was designed to quantify the best-case probability of intercepting a local three-dimensional anomaly between the lines. The anomaly is represented using a circular horizontal Gaussian footprint at a fixed target depth. Its quoted diameter D is the full width at half maximum, so the response sampled at horizontal distance d from the anomaly center is:

$$\frac{A(d)}{A_0} = \exp\left[-\frac{d^2}{2\sigma_h^{\,2}}\right] = 2^{-\frac{4d^2}{D^2}} \tag{7}$$

where:

$$\sigma_h = \frac{D}{2\sqrt{2\ln 2}} \tag{8}$$

For each anomaly center on a 0.01 m regular grid over the platform, the shortest distance to either diagonal is computed, and the maximum idealized line response is evaluated. A half-amplitude interception is defined as $A/A0 \geq 0.5$, which is equivalent to $d \leq D/2$. Diameters from 2 to 16 m were tested.

This experiment deliberately isolates observation geometry. It assumes that an anomaly produces a local response centered on its actual position and therefore does not simulate elastic wave propagation, scattering, spectral leakage, or the subsequent inversion. Its detectability is consequently an optimistic upper bound: a body missed by this geometry cannot be recovered from the two profiles alone, while a body geometrically intercepted may still be difficult to identify when its physical impedance contrast or spectral response is weak. The results are reported in Section 4.5 and were used only to define the spatial sampling limitation of the diagonal design.

3.4. Terrain-adaptive optimization of acquisition parameters

The acquisition parameters of the seismic frequency imaging technique—recording duration and receiver spacing—directly affect data quality and imaging resolution. These parameters are usually chosen on the basis of empirical values, but the Minhou work area is characterized by complex mountainous terrain, with strong topographic relief, uneven weathering-layer thickness, locally developed fracture zones, and relatively strong background-noise energy. A systematic optimization of these parameters under such conditions is therefore needed to balance imaging accuracy against operational efficiency.

3.4.1. Acquisition duration

Using line SK1-5-12 as an example, the imaging results for three recording durations—10 min, 20 min, and 30 min—were compared (Figure 4, Table 1). With 30 s Hann windows and 50% overlap, these records contain 39, 79, and 119 windows, respectively. If the window-to-window random component was treated as approximately independent, the

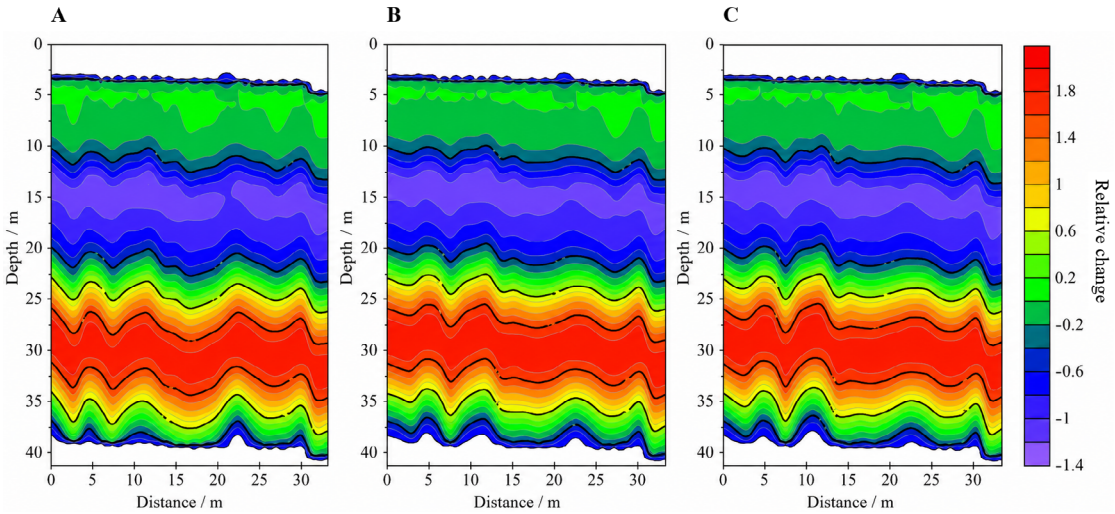


Figure 4. Comparison of seismic frequency imaging results for different acquisition durations: (A) 10 min, (B) 20 min, (C) 30 min. Colors represent relative imaging values, not lithology classes; lithologic interpretation requires borehole calibration.

Table 1. Qualitative evaluation of different acquisition durations

Evaluation criterion	10 min	20 min	30 min
Spectral stability	Poor	Good	Good
Profile SNR	Poor	Good	Good
Stratigraphic continuity	Fair	Good	Good
Interface clarity	Poor	Good	Good
Operational efficiency	Good	Fair	Poor
Overall recommendation	–	Recommended	–
30 s windows (50% overlap), *N*	39	79	119
Ideal random-stack factor, N−1/2	0.160	0.113	0.092

Notes: The good/fair/poor ratings are qualitative judgments based on the typical-line images and operational efficiency. *N* is the number of 30 s windows with 50% overlap; N−1/2 is shown only as an ideal random-noise benchmark because overlapped windows and persistent environmental noise are correlated.
Abbreviation: SNR: Signal-to-noise ratio.

standard error of a simple stack (scales as N−1/2) yielded relative factors of 0.160, 0.113, and 0.092. Thus, increasing duration from 10 to 20 min provides an idealized random-noise reduction by a factor of about 1.42, whereas increasing from 20 to 30 min yields only a further factor of about 1.23. Consistent with this expectation, the 10 min profile has poorer spectral stability and stratigraphic continuity; the 20 min profile is markedly clearer, and the 30 min result is visually similar to the 20 min result. Considering both imaging quality and operational efficiency, 20 min was adopted for this site. The N−1/2 calculation is a sampling benchmark rather than a guarantee because adjacent overlapped windows and persistent cultural sources are not statistically independent.

3.4.2. Receiver spacing

Using line SK66 as an example, the imaging results for three receiver spacings—1 m, 2 m, and 3 m—were compared (Figure 5). With a 3 m spacing, the layer interfaces were generally smooth, but the lateral sampling was sparse, and local detail was lost; a 2 m spacing characterized the principal interfaces broadly adequately; and as the spacing decreased, the accuracy of the lateral characterization improved, so that a 1 m spacing can clearly resolve small-scale lateral anomalies within the weathered layer. It must be stressed that the receiver spacing mainly affects the lateral characterization (the lateral resolution), whereas the vertical resolution is determined by the effective bandwidth and the inter-layer impedance contrast; the two

should not be confused, and reducing the spacing does not directly improve the vertical resolution. Taking the resolution requirements and the operational cost together, a 1 m spacing was adopted for fine tower-foundation detection in this work area. A qualitative evaluation of the three spacings is given in Table 2.

3.5. Field data acquisition

On the basis of the parameter optimization above, a 1 m receiver spacing and a 20 min recording duration per station were adopted as the principal acquisition parameters. In accordance with the characteristics of the Minhou work area, three survey grids—SK66, SK57-58, and SK1-5-12—were deployed; each grid comprised a pair of diagonal-crossing lines (designated line 1 and line 2), each line contained 23 stations, and 138 stations were acquired in total. Data were acquired with Gseis-3C integrated node seismographs, each housing a 5 Hz three-component vertical-orthogonal moving-coil geophone with a 32-bit high-precision analog-to-digital converter; the sampling rate was set to 500 Hz, the passband was 1–150 Hz, and the geophone sensitivity was about 84 V/(m/s). Both the horizontal and vertical ground-velocity signals were recorded and stored as raw time series.

Field acquisition followed a standardized protocol: station positions were set out accurately, positioning errors were controlled, and where terrain was difficult, the grid was adjusted appropriately and the actual coordinates recorded. Before acquisition, the instruments were well coupled, leveled, and time-synchronized, and during recording, regular artificial vibration was kept to a minimum within 100 m of the array. To ensure data quality and the reliability and comparability of the survey results, a rapid instrument-consistency check was performed every 24 h during the formal acquisition period.

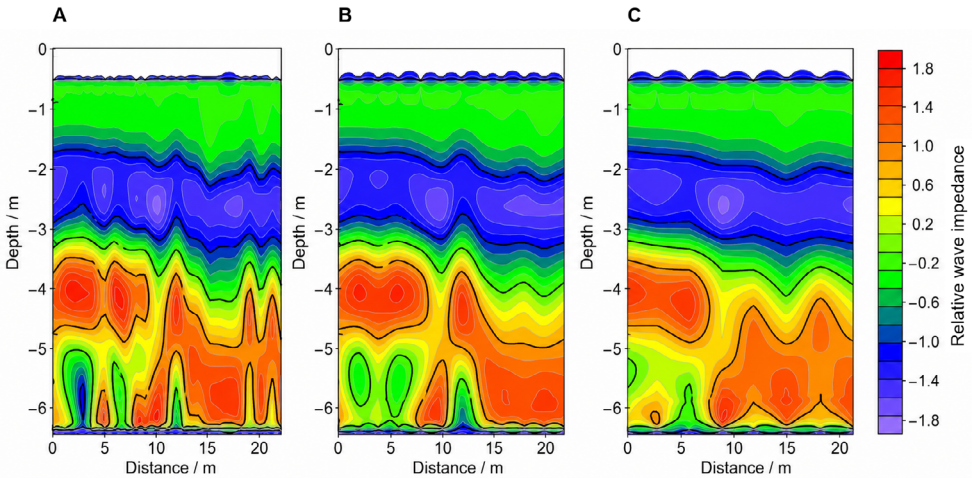


Figure 5. Comparison of seismic frequency imaging results for different receiver spacings: (A) 1 m, (B) 2 m, (C) 3 m. Colors represent relative wave-impedance contrast, not lithology classes; lithologic interpretation requires borehole calibration.

Table 2. Qualitative evaluation of different receiver spacings

Evaluation criterion	1 m	2 m	3 m
Lateral resolution	Good	Fair	Poor
Small-scale anomaly detection	Good	Fair	Poor
Interface continuity	Good	Good	Good
Station count and workload	High	Medium	Low
Operational efficiency	Fair	Good	Good
Overall recommendation	Recommended	–	–
Spatial Nyquist wavelength, 2Δx (m)	2	4	6

Notes: Receiver spacing chiefly controls lateral sampling. The 2Δx values are geometric Nyquist wavelengths for uniform sampling and do not represent vertical resolution or guarantee recovery of an interface at that wavelength; actual recoverability also depends on signal bandwidth, contrast, and processing.

4. Results

4.1. Data processing

Taking the target detection depth, regional velocities, and background-noise spectra together, the effective processing band was set to 1–40 Hz. The raw data first underwent waveform quality control to remove bad traces and records that did not reach the required duration, followed by a 1–40 Hz zero-phase band-pass filter. The multi-constrained workflow of Section 3.2 was then applied: 30 s Hann-window spectral estimation, spectral-stability screening, geological-prior constraints, and layer stripping were used to select characteristic frequencies and convert them to interface depths. The depths and inter-layer relative elastic contrasts were interpolated to dimensionless normalized relative wave-impedance profiles and interpreted jointly with regional geology and borehole logs. The borehole comparison in Section 4.3 provides an empirical interface-depth accuracy (root mean square error [RMSE] 0.61 m; mean absolute error [MAE] 0.53 m) for this field dataset; intrinsic vertical resolving power depends on bandwidth, impedance contrast, and the validity of the resonance approximation and therefore is not represented by a single universal value.

4.2. Imaging results

After processing, normalized relative wave-impedance profiles ranging from −10 to 10 (dimensionless) were obtained for each survey grid. The profiles use a blue–red color scale to represent the normalized relative wave impedance, with blue denoting relatively low values and red relatively high values. In each profile, the black arrow marks the position of the intersection of the two lines, the black vertical bar marks the position and depth of a borehole, and the black dashed lines (①, ②, ③) mark the principal wave-impedance interfaces, corresponding to the shallow, middle, and deep interfaces, respectively. It should be noted that the color scale reflects only the relative magnitude of the wave impedance; lithological interpretation must draw on the borehole data and cannot be based on color alone.

4.2.1. Survey grid SK66

The borehole of grid SK66 is located at the intersection of the two lines (Figure 6). The relative wave-impedance interface depths agree at the intersection of the two profiles, indicating reliable imaging with good closure. The layering is relatively clear: a shallow layer of relatively medium impedance about 5–10 m thick is underlain by a layer of relatively low impedance about 5–15 m thick, beneath which lies a layer of relatively high impedance about 10–15 m thick, while the top of the basal layer of relatively medium-to-high impedance lies at a depth of about 28 m and is laterally continuous and stable. Notably, a band of relatively low impedance is developed at depths of 25–35 m, corresponding to a local low-velocity zone; taking its spatial extent into account, it is tentatively attributed to local deepening of weathering, increased fracturing, or a change in water content, and is flagged for follow-up checking. The good closure of the interface depths at the intersection of the two lines validates the repeatability of two-dimensional profile imaging within a narrow work area.

4.2.2. Survey grid SK57-58

The boreholes of grid SK57-58 are located at the two endpoints of line 1 (Figure 7). The interface variations are consistent where the two profiles cross, and the imaging is reliable. The profiles are dominated by relatively low-impedance anomalies and are broadly gently undulating, displaying a clear four-layer structure in the vertical direction: above a depth of 13 m a layer of relatively medium impedance (−2 to 3) is interpreted, together with the borehole, as fill and silty clay; from 13 to 23 m a layer of relatively low impedance (−9 to −2) corresponds to completely weathered tuff; from 23 to 30 m a layer of relatively high impedance (2 to 9) corresponds to strongly weathered tuff; and below 30 m a layer of relatively medium-to-high impedance (0 to 9) corresponds to moderately weathered bedrock. This four-layer structure agrees well with the stratigraphic sequence revealed by boreholes SK57 and SK58 and fully reflects the weathering sequence from the overburden to moderately weathered bedrock.

4.2.3. Survey grid SK1-5-12

Grid SK1-5-12 is located in mountainous terrain with complex surface conditions (Figure 8). Within the small work area, the elevation along the diagonals varies considerably: line 1 has pronounced surface relief, whereas line 2 is generally gentle but develops a steep scarp at its end, with a maximum internal elevation difference of about 19 m. The boreholes of this grid are located at the endpoint of line 1 and at the line intersection. The stratigraphic structure along the two lines is fairly uniform, the most characteristic feature being a layer of relatively medium-to-high impedance (0 to 5) at a depth of 10–15 m; this is overlain by a region of relatively medium-to-low impedance (−2 to 1), underlain by a region of relatively low impedance (−5 to 2) at 15–25 m, and by a layer of relatively high impedance (0 to 9) below 25 m. Despite the strong surface relief, the underlying weathering interfaces and the top of the moderately weathered bedrock remain continuous and show no obvious systematic distortion caused by surface topography, indicating that the method adapts well to complex terrain.

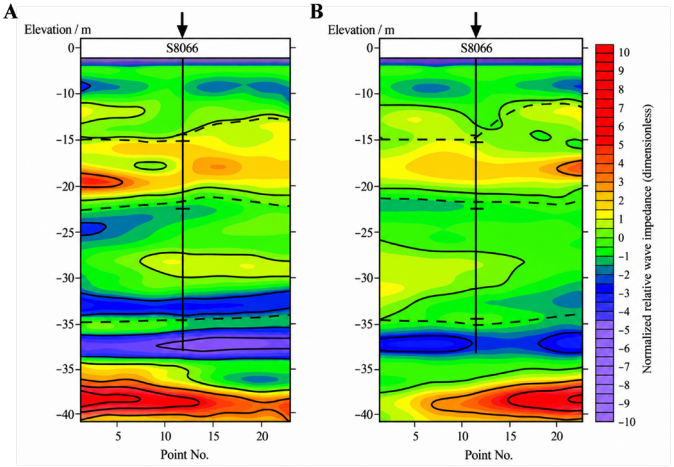


Figure 6. Seismic frequency imaging profiles of survey grid SK66: (A) line 1; (B) line 2. Colors represent profile-normalized relative wave impedance, not lithology classes; lithologic interpretation requires borehole calibration.

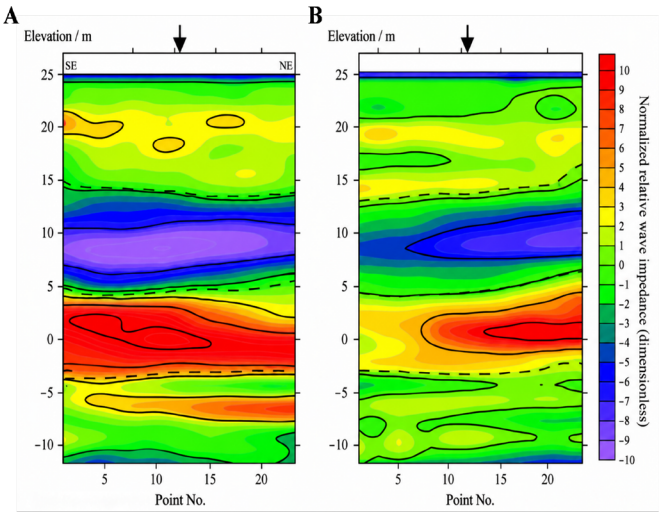


Figure 7. Seismic frequency imaging profiles of survey grid SK57-58: (A) line 1; (B) line 2. Colors represent profile-normalized relative wave impedance, not lithology classes; lithologic interpretation requires borehole calibration.

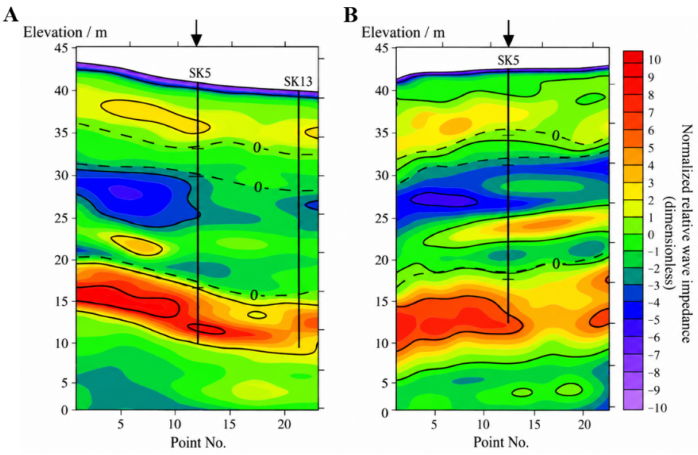


Figure 8. Seismic frequency imaging profiles of survey grid SK1-5-12: (A) line 1; (B) line 2. Colors represent profile-normalized relative wave impedance, not lithology classes; lithologic interpretation requires borehole calibration.

4.3. Borehole validation and error analysis

To evaluate quantitatively the accuracy with which the technique identifies the depths of stratigraphic interfaces, the principal wave-impedance interfaces marked by black dashed lines in the profiles (interfaces ①, ②, and ③, corresponding to the bottoms of the silty clay, the completely weathered layer, and the strongly weathered layer, respectively) were compared with the corresponding layer-bottom elevations revealed from five boreholes (Table 3). None of the boreholes penetrated the moderately weathered tuff, and its base is therefore unknown, so it does not take part in the depth validation. The imaged interface depths agree well with the borehole depths: across the 13 interface comparisons, the signed interpretation errors range from −0.80 to 1.20 m, with an RMSE of 0.61 m and an MAE of 0.53 m, and most interface errors are smaller than ±1.0 m.

The error distribution shows that the interpretation errors of the shallow interface (①) are generally positive and relatively stable, which may be related to the loose shallow fill and the larger lateral velocity variation, whereas the error of the deep interface (③) is larger at a few boreholes (for example, 1.20 m at SK5), tentatively attributed to the reduced inter-layer impedance contrast at depth and the increased uncertainty of characteristic-frequency picking. Overall, this accuracy meets the engineering requirements for bearing-stratum identification and uneven-foundation evaluation at mountainous tower sites, indicating that the method provides sufficient interface-resolution capability for engineering interpretation under complex terrain conditions.

On the basis of the borehole core logs, the normalized relative wave-impedance values over each depth interval were compared with lithology to establish an empirical correspondence for the study area (Table 4): the relatively low-impedance interval (−10 to −4) corresponds to completely weathered tuff, the relatively medium-impedance interval (−4 to 2) to silty clay or strongly weathered tuff, and the relatively high-impedance interval (2 to 10) to moderately weathered tuff (bedrock). This correspondence provides a quantitative reference for subsequent engineering-geological interpretation. It should be noted that the normalized relative wave impedance is a per-profile dimensionless relative value, and the same numerical interval may correspond to different lithologies in different profiles (for example, strongly weathered tuff appears as relatively high impedance in the SK57-58 profile); lithological interpretation must therefore be calibrated against borehole cores, and the associated non-uniqueness is discussed further in Section 5.5.

Table 3. Comparison between the seismic frequency imaging results and the borehole data

Borehole	Lithology	Layer-bottom elevation (m)	Interface	Interpretation error (m)
SK66	Silty clay	−10.30	①	+0.50
	Completely weathered tuff	−13.00	②	+0.60
	Strongly weathered tuff	−30.70	③	−0.15
SK5	Silty clay	27.70	①	+0.25
	Completely weathered tuff	24.50	②	+0.50
	Strongly weathered tuff	10.80	③	+1.20
SK12	Strongly weathered tuff	9.00	③	+0.10
SK57	Silty clay	13.20	①	+0.70
	Completely weathered tuff	4.30	②	−0.40
	Strongly weathered tuff	−5.00	③	−0.80
SK58	Silty clay	12.70	①	+0.70
	Completely weathered tuff	4.30	②	−0.80
	Strongly weathered tuff	−4.60	③	−0.20

Notes: Interpretation error = imaged interface elevation − borehole interface elevation (positive values indicate that the imaged interface is higher). Interfaces ①, ②, and ③ correspond to the bottoms of the silty clay, the completely weathered tuff, and the strongly weathered tuff, respectively. Error range −0.80 to 1.20 m; root mean square error [RMSE] = 0.61 m; mean absolute error [MAE] = 0.53 m (n = 13).

Table 4. Site-specific empirical association between normalized relative wave impedance and lithology

Normalized relative wave impedance (dimensionless)	Corresponding lithology
Relatively low impedance (−10 to −4)	Completely weathered tuff
Relatively medium impedance (−4 to 2)	Silty clay / strongly weathered tuff
Relatively high impedance (2 to 10)	Moderately weathered tuff (bedrock)

Notes: The normalized relative wave impedance is a per-profile dimensionless relative value. These intervals summarize the dominant associations in the Minhou borehole-calibrated data and must not be used as lithology-classification thresholds. Section 4.6 quantifies the substantial overlap risk; lithologic interpretation requires borehole calibration.

4.4. Sensitivity and uncertainty analysis

The 13 borehole residuals quantify total prediction error but do not, by themselves, identify independent contributions from ambient noise, velocity-prior bias, characteristic-frequency ambiguity, and spatial sampling, because these factors co-vary and no repeated controlled experiment exists for every borehole. A formal variance partition would therefore be unsupported. Instead, isolated perturbation tests were carried out to establish physically interpretable sensitivity coefficients and to compare their scale with the observed 0.61 m RMSE.

For **Equation 2**, a systematic shear-wave-velocity prior bias of ±5% or ±10% produces the same relative thickness bias; at a 20 m interface, this corresponds to approximately ±1.0 or ±2.0 m. A characteristic-frequency bias is nonlinear: a +5% frequency shift gives −4.8% thickness error (−0.95 m at 20 m), while a −5% shift gives +5.3% (+1.05 m). Noise affects the solution mainly by destabilizing the spectral peak; the duration test in Section 3.4.1 shows that ideal random-stack uncertainty fell from 0.160 for 10 min to 0.113 for 20 min and only to 0.092 for 30 min, consistent with diminishing returns after 20 min.

To isolate the effect of lateral sampling, a sinusoidal interface:

$$h(x) = A \sin\left(\frac{2\pi x}{\lambda} + \varphi\right) \tag{9}$$

with A = 1 m sampled over a 22 m line at spacings of 1, 2, and 3 m and reconstructed using linear interpolation. The RMSE was averaged over 360 phases φ. For λ = 4 m, the RMSE values were 0.15, 0.48, and 0.84 m; for λ = 8 m, 0.04, 0.15, and 0.31 m; and for λ = 12 m, 0.02, 0.07, and 0.15 m. At the selected 1 m spacing, geometric interpolation error was therefore ≤0.15 m for this test when $\lambda \geq 4$ m, well below the field RMSE. The sensitivity ranking suggests that, after SNR screening and at 1 m spacing, uncertainty in velocity calibration and characteristic-frequency assignment/non-uniqueness is more capable of generating meter-scale vertical errors than lateral sampling alone. This is a scale comparison, not a statistical attribution of percentages to each error source.

4.5. Geometry-only synthetic response of local three-dimensional bodies

The geometry test described in Section 3.3 quantifies the fraction of potential anomaly-center locations whose Gaussian footprint is intercepted by either diagonal at least half of its peak response. The half-amplitude interception probability was 24.1% for D = 2 m, 44.8% for 4 m, 62.3% for 6 m, 76.4% for 8 m, 87.3% for 10 m, 94.8% for 12 m, 99.0% for 14 m, and 100% for 16 m (Figure 9). Hence, in the purely geometric best case, a 4 m-diameter boulder or pocket-shaped weathering body located arbitrarily within the platform is missed by the half-amplitude criterion more than half of the time, whereas a footprint of about 12 m is required for approximately 95% interception. The mean maximum line response rose from 25.0% of anomaly peak at D = 2 m to 84.3% at D = 12 m.

These values define only a sampling scale for the two-line geometry. They do not imply that all intercepted bodies will be resolved in the frequency-imaging profile: weak impedance contrast, finite wavelength, spectral mixing, and inversion smoothing can reduce detectability further. Conversely, a broad anomaly can influence both lines even if its center lies between them. Therefore, the diagonal-crossing layout is suitable for checking laterally persistent interfaces and broad anomalies but cannot exclude small isolated three-dimensional bodies. Where boulders, pocket-shaped weathering bodies, or fracture zones are design-critical, the grid must be densified or complemented by drilling and genuinely three-dimensional geophysical acquisition.

4.6. Interval-overlap analysis of normalized relative wave impedance and lithology

The normalized relative wave impedance was scaled

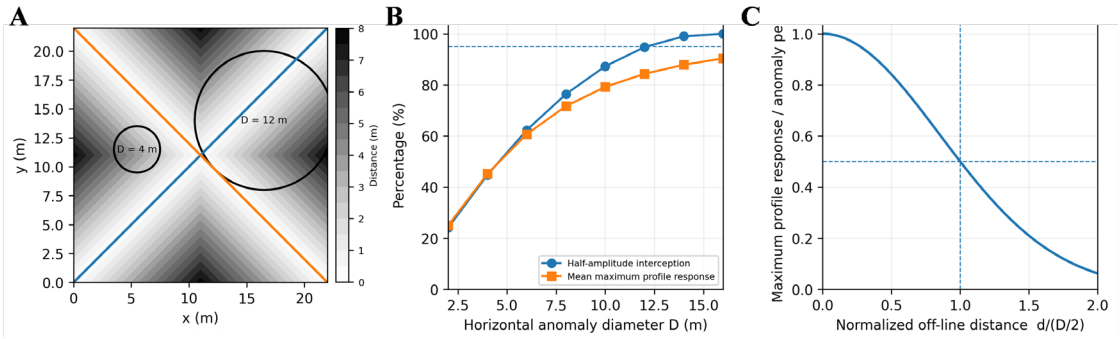


Figure 9. Geometry-only synthetic sampling test for a local three-dimensional Gaussian anomaly within a 22 m × 22 m tower platform: (A) distance to the nearest diagonal with illustrative 4 m and 12 m half-amplitude footprints; (B) half-amplitude interception probability and mean maximum line response versus anomaly diameter; (C) idealized Gaussian line response versus normalized off-line distance. The test is an optimistic sampling bound and does not simulate elastic wave propagation or inversion.

independently for each profile, so its numerical values cannot be treated as universal lithology thresholds. To make the overlap risk explicit, the lithology-specific ranges described for the SK57-58 profile were compared: silty clay −2 to 3, completely weathered tuff −9 to −2, strongly weathered tuff 2 to 9, and moderately weathered tuff 0 to 9. For two intervals *Ri* and *Rj*, an overlap index:

$$O_{ij} = \frac{\left|R_i \cap R_j\right|}{\min\left(\left|R_i\right|, \left|R_j\right|\right)} \tag{10}$$

was calculated, with boundary-only contact assigned zero overlap. Three of the six lithology pairs had non-zero overlap. The three non-zero overlaps were $O = 0.20$ for silty clay versus strongly weathered tuff, $O = 0.60$ for silty clay versus moderately weathered tuff, and $O = 1.00$ for strongly versus moderately weathered tuff; in the last case, the entire strongly weathered interval lies inside the broader moderately weathered range. This directly demonstrates that color or normalized amplitude alone cannot provide unique lithological classification even within one profile.

5. Discussion

5.1. Methodological positioning relative to other near-surface methods

Natural-source seismic frequency imaging occupies a specific niche among near-surface methods, and clarifying its relationship to more established techniques helps delimit when it is the appropriate choice. Single-station microtremor and HVSR analyses[19-21] also exploit ambient vibration and require no active source, but they are designed mainly to estimate a fundamental site frequency or a one-dimensional velocity profile at a point and do not, by themselves, yield a laterally continuous section. The present technique retains the passive, source-free character of those methods while adding array observation and layer-stripping recursion, so that a continuous profile of the relative elastic structure is obtained and the cover and the completely, strongly, and moderately weathered layers can be tracked laterally. Multichannel analysis of surface waves (MASW)[22,23] likewise images the shear-wave velocity structure; however, because it relies on the inversion of dispersion curves, its vertical resolution degrades with depth and thin or gradational weathering interfaces are easily smoothed. Electrical methods such as high-density resistivity[4,5] are sensitive to moisture and clay content and are well suited to mapping water-bearing or strongly weathered zones, yet their shallow boundaries tend to be blurred at the scale of a single tower. By contrast, the frequency imaging used here is driven by the impedance contrast across interfaces and is therefore comparatively sensitive to the depth of distinct weathering boundaries, although it yields a relative rather than an absolute property and must be tied to boreholes for lithological meaning. These methods are thus complementary rather than competing: where the objective is to delineate the geometry of weathering interfaces beneath a small, hard-to-access footprint, the present technique is efficient, whereas a full characterization of a complex site may still benefit from combining it with surface-wave or electrical surveys.

For a systematic comparison, Table 5 summarizes the principal trade-offs among the present workflow, single-station HVSR/microtremor, MASW/surface-wave methods, and ambient-noise interferometry/tomography. Because these methods target different physical quantities, depths, apertures, and validation endpoints, the numerical entries are presented as method-specific context rather than a controlled head-to-head accuracy ranking.

The comparison clarifies that the novelty of this study is not the quarter-wavelength relation. It is the engineering integration of multi-window stability/SNR screening,

Table 5. Comparison of the proposed workflow with representative near-surface seismic methods

Method	Accuracy/Resolution	Field efficiency/Noise	Applicability/Limitation
Natural-source seismic frequency imaging (this study)	13 interfaces: RMSE 0.61 m, MAE 0.53 m; 1 m lateral sampling; vertical resolution depends on bandwidth and contrast.	Passive; 20 min/station; SNR/stability screening plus geological priors.	Small rugged tower sites; borehole-calibrated; quasi-2D and may miss off-line 3D bodies.
Single-station HVSR/ microtremor[19-21,25,26,32,33]	1D resonance/depth estimate; no lateral section; accuracy depends strongly on V_S and resonance validity.	Very low field burden; coherent or directional noise can bias peaks.	Rapid bedrock/resonance screening; requires velocity or borehole control.
MASW/Surface-wave methods[8,9,22,23,30,31,34]	V_S profile/section; resolution depends on wavelength, aperture, and spacing; thin interfaces may be smoothed.	Multichannel; active shots or longer passive records increase field workload.	Established V_S imaging; larger footprint and modal/source effects can limit small tower sites.
Ambient-noise interferometry/ tomography[17,28,29]	2D/3D velocity structure; resolution depends on spacing, frequency band, and path coverage.	Passive but requires many synchronized stations and long records.	Area-scale imaging; generally inefficient for a 22 m × 22 m tower footprint.

Notes: Only values measured in this study are reported as site-specific quantitative performance. The literature-based rows summarize method controls and limitations and are not intended as a head-to-head ranking because the target properties, apertures, and validation endpoints differ.
Abbreviations: HVSR: Horizontal-to-vertical spectral ratio; MAE: Mean absolute error; MASW: Multichannel analysis of surface waves; RMSE: Root mean square error; SNR: Signal-to-noise ratio; V_S: Shear velocity.

geological-prior constraints, and layer stripping with a two-diagonal closure-check geometry, site-tested acquisition parameters, borehole validation, and explicit sensitivity, non-uniqueness, and off-line three-dimensional sampling analyses. Relative to single-station HVSR, the workflow provides laterally continuous profiles; relative to surface-wave arrays, it reduces source and aperture demands for a small tower footprint, but it does not recover absolute V_S and remains dependent on borehole calibration. The resulting advantage is therefore application-specific rather than universal.

5.2. Adaptability of the multi-constrained extraction to complex ambient-noise conditions

Complex mountainous sites contain transient and persistent noise that can create spurious spectral peaks. The multi-window SNR/stability screen removes unstable candidates, the geological prior rejects physically implausible candidates, and layer stripping reduces masking of deeper responses. However, Section 4.4 shows why these controls do not eliminate uncertainty: after the 20 min stack stabilizes random fluctuations, a 5% velocity-prior or frequency-pick bias is already capable of producing about 1 m depth error at a 20 m interface. The slightly larger RMSE of interface ③ (0.66 m) is consistent with reduced deep contrast and more ambiguous peak assignment, although n is too small for formal attribution. The dominant controllable priorities are therefore local velocity/borehole calibration and transparent treatment of alternative spectral picks, rather than simply extending recording time. A biased prior can remove a genuine peak as readily as it can suppress a spurious one.

5.3. Effects of acquisition duration and receiver spacing

Acquisition duration and receiver spacing affect different parts of the workflow. Duration controls the number of spectral windows: the 20 min record contains 79 overlapped 30 s windows and captures most of the ideal stacking gain between the 10 and 30 min tests. Receiver spacing controls lateral sampling rather than vertical resolution. The sinusoidal-interface test shows that 1 m spacing contributes only 0.15 m phase-averaged geometric interpolation RMSE for a 4 m lateral wavelength and less for broader interfaces; 2–3 m spacing degrades small-scale recovery rapidly. The selected 1 m/20 min combination is therefore defensible for the Minhou field data but is not a universal optimum, because the required duration and spacing depend on local noise spectrum, velocity, target scale and impedance contrast.

5.4. Reliability and limitations of the diagonal-crossing lines

Agreement at line intersections provides a useful closure check for laterally persistent interfaces and confirms repeatability along the two sampled directions. It does not create true three-dimensional coverage. The geometry-only test in Section 4.5 makes this limitation quantitative: an arbitrarily located 4 m anomaly meets the half-amplitude interception criterion only 44.8% of the time, and a

footprint of about 12 m is required for ~95% interception under optimistic assumptions. Small boulders, pocket-shaped weathering bodies, or fracture zones between the diagonals can therefore be absent from both profiles without violating the line-crossing closure. This is a critical engineering limitation. If isolated three-dimensional hazards could control foundation design, the diagonal layout should be densified or combined with drilling and a genuinely three-dimensional geophysical method; the present two-line system cannot be used to rule them out.

5.5. Non-uniqueness of the normalized relative wave impedance

Normalized relative wave impedance is a per-profile dimensionless contrast measure, not an absolute material property. The quantified overlap in Section 4.6 shows the practical consequence: in SK57-58 the strongly weathered interval (2–9) is entirely contained in the reported moderately weathered interval (0–9), and the silty-clay interval overlaps 60% of the smaller interval with moderately weathered tuff. Accordingly, the principal defensible use of the color image is to locate and laterally track contrast boundaries after calibration; it is not a stand-alone lithology classifier. All profile captions now carry this warning. Cross-profile interpretation should use boreholes and, where possible, a site-unified velocity–impedance–lithology model.

5.6. Implications for power-transmission corridor investigation and conditions for wider use

For transmission corridors, the practical value of the technique is rapid, continuous screening between sparse boreholes: it can prioritize borehole locations, identify laterally changing interfaces, and flag positions that warrant targeted follow-up while avoiding active-source mobilization. Its appropriate role is therefore complementary. The method does not provide absolute V_S, absolute impedance, lithologic strength parameters, or a complete three-dimensional ground model; these quantities must come from independent geotechnical or geophysical constraints.

In the present Minhou trial, successful applications were obtained at detection depths of approximately 50 m or less and weathering-layer thicknesses of approximately 30 m or less; these values are site-specific empirical conditions rather than transferable applicability thresholds. Their validity depends on the target-band resonance remaining measurable, sufficient impedance contrast across the interface, the ambient-noise spectrum not being dominated by coherent cultural peaks, the local velocity structure satisfying the calibration, and the stratigraphic combination being simple enough for peak separation and layer stripping. A different mountainous region can violate any of these conditions even at shallower depth, or can remain usable at greater depth if contrast and low-frequency energy are favorable. Before transfer to a new corridor, a small number of boreholes should be used to establish the local velocity–frequency–thickness relation and to repeat short tests of recording duration, spacing and spectral stability. The Minhou settings and accuracy should not be transplanted without this calibration.

6. Conclusion

This study adapted natural-source seismic frequency imaging to small mountainous transmission-tower sites and evaluated both its field accuracy and its principal uncertainty/geometry limits. The conclusions are as follows.

(i) The field workflow combines multi-window spectral-stability screening, geological-prior constraints, and layer stripping with a two-diagonal observation geometry. At the Minhou site, 1 m station spacing and 20 min recording per station provided a practical balance between lateral sampling, spectral stability, and field workload.

(ii) Against 13 layer-bottom interfaces from five boreholes, signed errors range from −0.80 to 1.20 m, with RMSE 0.61 m and MAE 0.53 m. Interface-specific RMSE values are 0.57, 0.59, and 0.66 m for interfaces ①–③, respectively. Sensitivity tests show that a 5% velocity-prior or frequency-pick bias can generate approximately 1 m depth error at H = 20 m; thus, local velocity calibration and robust peak assignment can be more consequential for vertical uncertainty than the selected 1 m lateral spacing.

(iii) The displayed normalized relative wave impedance is a profile-normalized dimensionless contrast quantity. Substantial overlap of lithology-associated ranges occurs even within SK57-58 (overlap index 1.00 for strongly versus moderately weathered tuff), so color contours cannot be converted directly to lithology. Borehole calibration is required.

(iv) The diagonal-crossing geometry is quasi-two-dimensional and cannot exclude isolated three-dimensional bodies between the lines. In the geometry-only synthetic test, the half-amplitude interception probability is about 44.8% for a 4 m anomaly and reaches about 94.8% only at D = 12 m. These are optimistic sampling bounds; where boulders, pocket-shaped weathering bodies, or fracture zones are design-critical, denser, or genuinely three-dimensional acquisition and drilling are required.

(v) The approximately 50 m detection depth, 30 m

weathering thickness, 1 m spacing, and 20 min duration reported here are site-specific empirical settings, not universal criteria. Transfer to another mountainous region requires local borehole/velocity calibration and renewed checks of impedance contrast, noise spectrum, stratigraphic complexity, and acquisition parameters. Within these limits, the method is a practical continuous-coverage complement to drilling rather than a replacement for drilling or a universal lithology classifier.

Acknowledgments

The authors thank the field crews who assisted with data acquisition.

Funding

This research was funded by the Science and Technology Project of State Grid Fujian Electric Power Co., Ltd. (State Grid Fujian Economic Research Institute 2026 Project: Key Technologies and Equipment Development for Fully Localized Detection of Non-Metallic and Deep-Buried Pipelines in Power Grid Engineering; contract number SGFJJY00PWJS2600068).

Conflict of interest

Xiao Yang and Jiahui Zuo are employed by Geological Survey and Digital Earth (Beijing) Technology Co., Ltd.; however, they were not involved in any activities that could constitute a conflict of interest in relation to this study. The authors declare no other conflicts of interest.

Author contributions

Conceptualization: Wangxin Cai
Data curation: Xiao Yang
Formal analysis: Jiahui Zuo, Congyu Lin
Investigation: Wangxin Cai, Congyu Lin, Jiahui Zuo
Methodology: Xiao Yang
Software: Xiao Yang
Validation: Wangxin Cai, Congyu Lin, Xiao Yang
Visualization: Xiao Yang
Writing–original draft: Wangxin Cai
Writing–review & editing: Congyu Lin, Xiao Yang
All authors have read and approved the manuscript.

Availability of data

The data presented in this study are available from the corresponding authors upon reasonable request. The data are not publicly available because they were acquired for an engineering project of the State Grid and are subject to commercial-confidentiality restrictions.

Further disclosure

During the preparation of this manuscript, the authors used a large language model for English-language polishing only. The authors reviewed and edited the output and take full responsibility for the content of this manuscript.

References

1. Ibitoye FP, Ipinmoroti FV, Salami M, Akinluwade KJ, Taiwo AT, Adetunji AR. Application of geophysical methods to building foundation studies. *Int J Geosci*. 2013;4(9):1256-1266.

   doi: 10.4236/ijg.2013.49120

2. Zhu HH, Yan JX, Liang WH. Challenges and development prospects of ultra-long and ultra-deep mountain tunnels. *Engineering*. 2019;5(3):384-392.

   doi: 10.1016/j.eng.2019.04.009

3. Martínez K, Mendoza JA. Urban seismic site investigations for a new metro in central Copenhagen: near-surface imaging using reflection, refraction and VSP methods. *Phys Chem Earth Parts A/B/C*. 2011;36(16):1228-1236.

   doi: 10.1016/j.pce.2011.01.003

4. Lai WWL, Dérobert X, Annan P. A review of ground-penetrating radar application in civil engineering: a 30-year journey from locating and testing to imaging and diagnosis. *NDT E Int*. 2018;96:58-78.

   doi: 10.1016/j.ndteint.2017.04.002

5. Loke MH, Chambers JE, Rucker DF, Kuras O, Wilkinson PB. Recent developments in the direct-current geoelectrical imaging method. *J Appl Geophys*. 2013;95:135-156.

   doi: 10.1016/j.jappgeo.2013.02.017

6. Egbert GD. Robust multiple-station magnetotelluric data processing. *Geophys J Int*. 1997;130(2):475-496.

   doi: 10.1111/j.1365-246X.1997.tb05663.x

7. Weckmann U, Magunia A, Ritter O. Effective noise separation for magnetotelluric single-site data processing using a frequency-domain selection scheme. *Geophys J Int*. 2005;161(3):635-652.

   doi: 10.1111/j.1365-246X.2005.02621.x

8. Foti S, Hollender F, Garofalo F, et al. Guidelines for the good practice of surface wave analysis: a product of the InterPACIFIC project. *Bull Earthquake Eng*. 2018;16(6):2367-2420.

   doi: 10.1007/s10518-017-0206-7

9. Socco LV, Foti S, Boiero D. Surface-wave analysis for building near-surface velocity models—established approaches and new perspectives. *Geophysics*. 2010;75(5):75A83-75A102.

   doi: 10.1190/1.3479491

10. Solla M, Pérez-Gracia V, Fontul S. A review of GPR application on transport infrastructures: troubleshooting and best practices. *Remote Sens*. 2021;13(4):672.

doi: 10.3390/rs13040672

11. Capozzoli L, Rizzo E. Combined NDT techniques in civil engineering applications: laboratory and real test. *Constr Build Mater*. 2017;154:1139-1150.

doi: 10.1016/j.conbuildmat.2017.07.147

12. Qin H, Xie X, Vrugt JA, Zeng K, Hong G. Underground structure defect detection and reconstruction using crosshole GPR and Bayesian waveform inversion. *Autom Constr*. 2016;68:156-169.

doi: 10.1016/j.autcon.2016.03.011

13. Romero-Ruiz A, Linde N, Keller T, Or D. A review of geophysical methods for soil structure characterization. *Rev Geophys*. 2018;56(4):672-697.

doi: 10.1029/2018RG000611

14. Wadas S, Polom U, Krawczyk CM. High-resolution shear-wave seismic reflection as a tool to image near-surface subrosion structures—a case study in Bad Frankenhausen, Germany. *Solid Earth*. 2016;7(5):1491-1508.

doi: 10.5194/se-7-1491-2016

15. Picozzi M, Parolai S, Bindi D, Strollo A. Characterization of shallow geology by high-frequency seismic noise tomography. *Geophys J Int*. 2009;176(1):164-174.

doi: 10.1111/j.1365-246X.2008.03966.x

16. Malehmir A, Durrheim R, Bellefleur G, et al. Seismic methods in mineral exploration and mine planning: a general overview of past and present case histories and a look into the future. *Geophysics*. 2012;77(5):WC173-WC190.

doi: 10.1190/geo2012-0028.1

17. Lin FC, Li D, Clayton RW, Hollis D. High-resolution 3D shallow crustal structure in Long Beach, California: application of ambient noise tomography on a dense seismic array. *Geophysics*. 2013;78(4):Q45-Q56.

doi: 10.1190/GEO2012-0453.1

18. Pazzi V, Di Filippo M, Di Nezza M, *et al*. Integrated geophysical survey in a sinkhole-prone area: microgravity, electrical resistivity tomographies, and seismic noise measurements to delimit its extension. *Eng Geol*. 2018;243:282-293.

doi: 10.1016/j.enggeo.2018.07.016

19. Lermo J, Chávez-García FJ. Site effect evaluation using spectral ratios with only one station. *Bull Seismol Soc Am*. 1993;83(5):1574-1594.

doi: 10.1785/BSSA0830051574

20. Molnar S, Cassidy JF, Castellaro S, et al. Application of microtremor horizontal-to-vertical spectral ratio analysis for site characterization: state of the art. *Surv Geophys*. 2018;39(4):613-631.

doi: 10.1007/s10712-018-9464-4

21. Xu R, Wang L. The horizontal-to-vertical spectral ratio and its applications. *EURASIP J Adv Signal Process*. 2021;2021:75.

doi: 10.1186/s13634-021-00765-z

22. Park CB, Miller RD, Xia J. Multichannel analysis of surface waves. *Geophysics*. 1999;64(3):800-808.

doi: 10.1190/1.1444590

23. Xia J, Miller RD, Park CB. Estimation of near-surface shear-wave velocity by inversion of Rayleigh waves. *Geophysics*. 1999;64(3):691-700.

doi: 10.1190/1.1444578

24. Asten MW, Henstridge JD. Array estimators and the use of microseisms for reconnaissance of sedimentary basins. *Geophysics*. 1984;49(11):1828-1837.

doi: 10.1190/1.1441596

25. Molnar S, Sirohey A, Assaf J, *et al*. A review of the microtremor horizontal-to-vertical spectral ratio method. *J Seismol*. 2022;26(4):653-685.

doi: 10.1007/s10950-021-10062-9

26. Sgattoni G, Castellaro S. Detecting 1-D and 2-D ground resonances with a single-station approach. *Geophys J Int*. 2020;223(1):471-487.

doi: 10.1093/gji/ggaa325

27. Bonnefoy-Claudet S, Cotton F, Bard PY. The nature of noise wavefield and its applications for site effects studies: a literature review. *Earth Sci Rev*. 2006;79(3-4):205-227.

doi: 10.1016/j.earscirev.2006.07.004

28. Campillo M, Paul A. Long-range correlations in the diffuse seismic coda. *Science*. 2003;299(5606):547-549.

doi: 10.1126/science.1078551

29. Shapiro NM, Campillo M, Stehly L, Ritzwoller MH. High-resolution surface-wave tomography from ambient seismic noise. *Science*. 2005;307(5715):1615-1618.

doi: 10.1126/science.1108339

30. Socco LV, Strobbia C. Surface-wave method for near-surface characterization: a tutorial. *Near Surf Geophys*. 2004;2(4):165-185.

doi: 10.3997/1873-0604.2004015

31. Foti S, Lai CG, Rix GJ, Strobbia C. *Surface Wave Methods for Near-Surface Site Characterization*. Boca Raton, FL: CRC Press; 2014.

doi: 10.1201/b17268

32. Bignardi S. The uncertainty of estimating the thickness of soft sediments with the HVSR method: a computational

point of view on weak lateral variations. *J Appl Geophys*. 2017;145:28-38.

doi: 10.1016/j.jappgeo.2017.07.017

33. Moon SW, Subramaniam P, Zhang Y, Vinoth G, Ku T. Bedrock depth evaluation using microtremor measurement: empirical guidelines at weathered granite formation in Singapore. *J Appl Geophys*. 2019;171:103866.

doi: 10.1016/j.jappgeo.2019.103866

34. Baglari D, Dey A, Taipodia J. A state-of-the-art review of passive MASW survey for subsurface profiling. *Innov Infrastruct Solut*. 2018;3:66.

doi: 10.1007/s41062-018-0171-2